V European Conference on Computational Fluid Dynamics
ECCOMAS CFD 2010
J. C. F. Pereira and A. Sequeira (Eds)
Lisbon, Portugal,14-17 June 2010

NUMERICAL SIMULATION OF AN ELECTRIC CHARGED COMPRESSIBLE GAS-FLOW WITH ADAPTIVE MESH REFINEMENT

S. Reichel, R. Groll, H.J. Rath

ZARM - University of Bremen
Am Fallturm, D-28359 Bremen, Germany
e-mail: reichel@zarm.uni-bremen.de
e-mail: groll@zarm.uni-bremen.de

Key words: adaptive mesh, sonic flow, shock wave, expansion flow

Abstract. *In this paper, a computational method for modeling the behavior of a dilute gas flow is presented. The Navier-Stokes equation and the Lorentz force (electrical volume force depending on the charge of the gas flow, electric and magnetic field intensities) are used for the development of the present solver. The results are validated on the experimental data.*
The environmental pressure of the present test case is in the range of 0.1 up to 100 Pa. The electrical power is in a range of 100 and 200 W. The propulsion system operates steady-state. Argon and Xenon are the common used propellants.
An additional feature of the new solver is the adaptive mesh refinement tool. The simulation results of this adaptive refinement tool are shown. The refinement tool increases the local number of cells for high resolved solutions by only a minor of numerically extend.

NOMENCLATURE

$\dot{V}$	volume flow	V	volume
ρ	density	p	pressure
$\vec{v}$	velocity	e	internal energy
α	heat conductivity	R_0	ideal gas constant
M	molar mass	T	temperature
c_v	isochoric heat capacity	μ	dynamic viscosity

Table 1: nomenclature

1 INTRODUCTION

Electric propulsion systems and the behavior of dilute gases have been subjects in many studies. T.S. Sheshadri [1] investigated the thrust for different propellants and operating temperatures, E. Choueiri [2] formulated empirically-based model for the description of MPD-Thrusters, R.Groll [3] molecular dynamic transport in microchannels, R.M. Meyers [4] characterized scaling laws and A. Fruchtman the influence of the Thruster geometry [5].

In this paper, the subject of interest is the definition of a 3D numerical computer model. For this propose, a standard solver is used and modified to describe the behavior of a dilute gas flow through a nozzle. The solution of the new solver is validated on experimental data. The visible advantage of the new solver is an adaptive mesh refinement tool. This tool increases the local number of cells for higher resolved solutions by a minimum of numerical extend.

2 EXPERIMENTAL SETUP

The experimental setup, see figure 1, is embedded into a vacuum chamber. During the experiments the pressure inside this chamber is in the range of 0.1 to 100 Pa, the electrical power of 100 to 200 W. The propulsion system operates steady-state. Argon and Xenon are the commonly used propellants. The anode plate is convertible. In this way, the concentric rift between the anode and the cathode is variable.

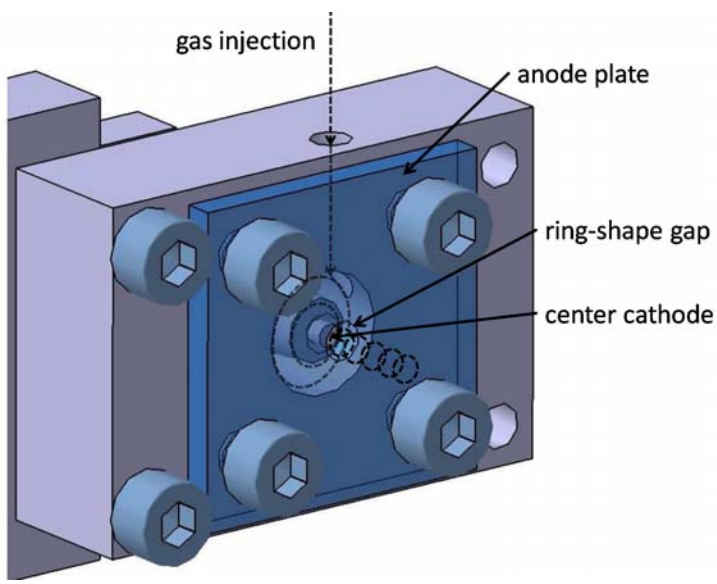

Figure 1: First experimental setup - concentric rift and convertable anode plate (transparent)

During the cunducted experiments the Argon gas flow (from 0.2 up to 1.8 Nl/min) and the current (from 0.03 up to 0.15 A) through the concentric rift was modified. Hence the operating voltage between the anode and the cathode was adjusted by ambient conditions and measured with a corresponding electrical measurement technique. The results for an Argon gas flow is pictured in the plot below, see figure 2.

The plot shows the relation between the argon mass flow and the "burning voltage" through the plasma. The preset current during the different experimental runs was fixed, the gas flow was modified. The plot, of figure 2, shows a decreasing "burning voltage" for higher volume flows $\frac{dV}{dt}$. The experiments have been repeated with several different preset currents. The result shows for higher preset currents higher "burning voltages". That means, the electrical resistant of the experimental setup does not depend on the preset current, but on the gas flow rates. Higher flow rates cause a decrease of the electrical resistance of the system. The plot, figure 2, includes five additional pictures of the working experimental setup.

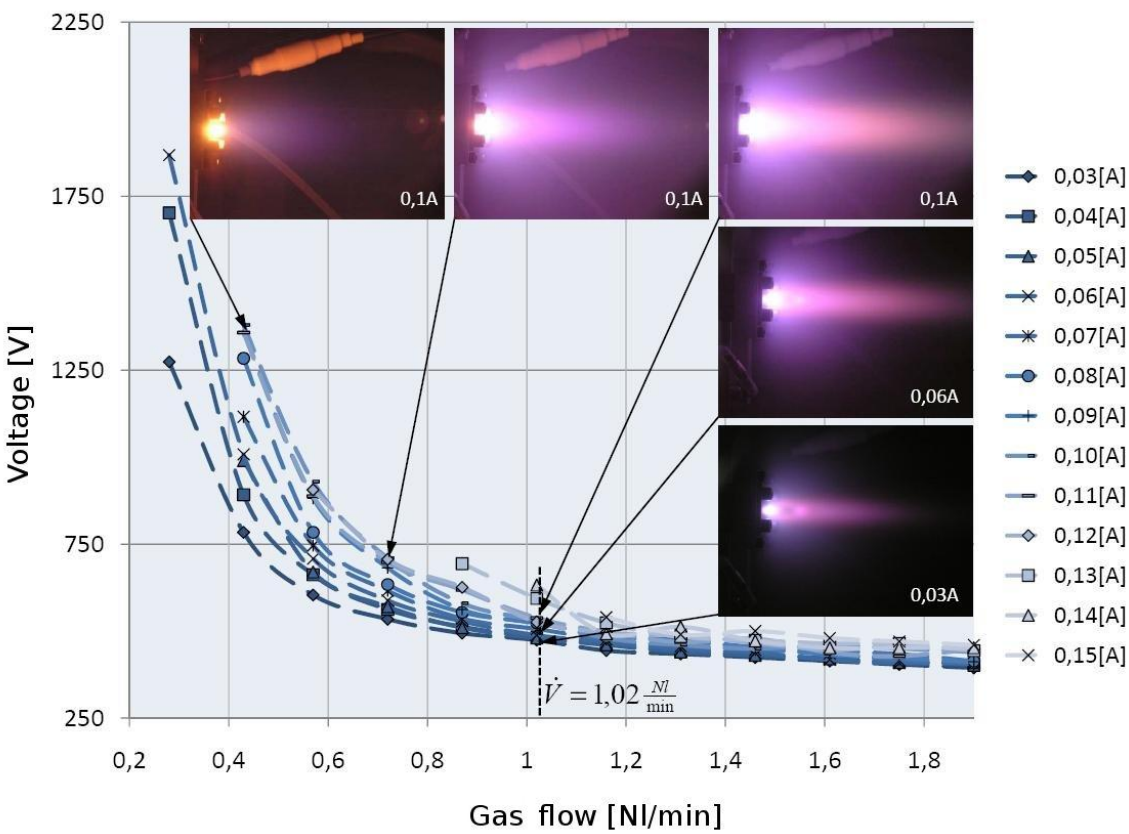

Figure 2: results of te experiment / relation between gas-flow and voltage between anode and cathode

3 NUMERICAL METHODS

A simplified mesh model of the experimental setup is used for the validation of the numerical simulation. The first simulations where conducted with a basic compressible sonic solver. This standard solver solves the compressible Navier-Stokes equation, the mass continuity equation and the energy equation [7]. A PISO loop for algorithms control is included. The used equations are enlisted below.

compressible Navier-Stokes equation

$$\frac{\partial}{\partial t}(\rho\vec{v}) + \nabla\cdot(\rho\vec{v}\vec{v}) - \nabla\cdot\left[\mu(\nabla\vec{v} + (\nabla\vec{v})^T)\right] + \nabla\cdot\left[\frac{2}{3}\mu(\nabla\cdot\vec{v})tr\right] = -\nabla p \tag{1}$$

mass continuity equation

$$\frac{\partial\rho}{\partial t} + \nabla\cdot(\rho\vec{v}) = 0 \tag{2}$$

energy equation

$$\frac{\partial}{\partial t}(\rho e) + \nabla\cdot(\rho\vec{v}e) - \nabla(\alpha\nabla e) = -p(\nabla\cdot\vec{v}) \tag{3}$$

ideal gas law

$$\frac{p}{\rho} = \frac{R_0}{M}T \tag{4}$$

heat capacity

$$T = \frac{e - e_0}{c_v} \tag{5}$$

The dynamic viscosity is given by the Sutherland transport model [6]

$$\mu = \frac{A_s\cdot T^{\frac{3}{2}}}{T + T_s} \tag{6}$$

For higher resolved solutions and 3D simulations the solver is modified. The additional feature of the modified solver is the adaptive mesh refinement tool. In this way the solver is able to refine and unrefine "critical" and "subcritical" cells. The basic idea of the new solver is to define a simple mesh with a few thousand cells within the solver is able to generate a high resolved solution by using a minimum of system sources (memory and processor time).

In opposing to the basic solver the requirements of the new solver has changed. The refinement solver needs a hexametric mesh and asymmetric boundary conditions. Additional solver settings for the refinement description are necessary.

The refinement options are defined in a separated refinement data set. One of the refinement options is the refinement interval. If it was set to 1 the mesh would be modified

every time step. Such a setting is not favorable, because the mesh generations slow down the iteration process. If the refinement interval is too large, the final process solution needs too many iteration steps. For compressible dilute supersonic gas flows, the common refinement interval ranges from 40 and 100 time steps.
Another important setting in the refinement options is the refinement threshold. Basically the cell refinement is coupled to the density gradient ($\nabla\rho$). If the density gradient in any cell reaches the critical value, the solver selects this cell for decomposition.

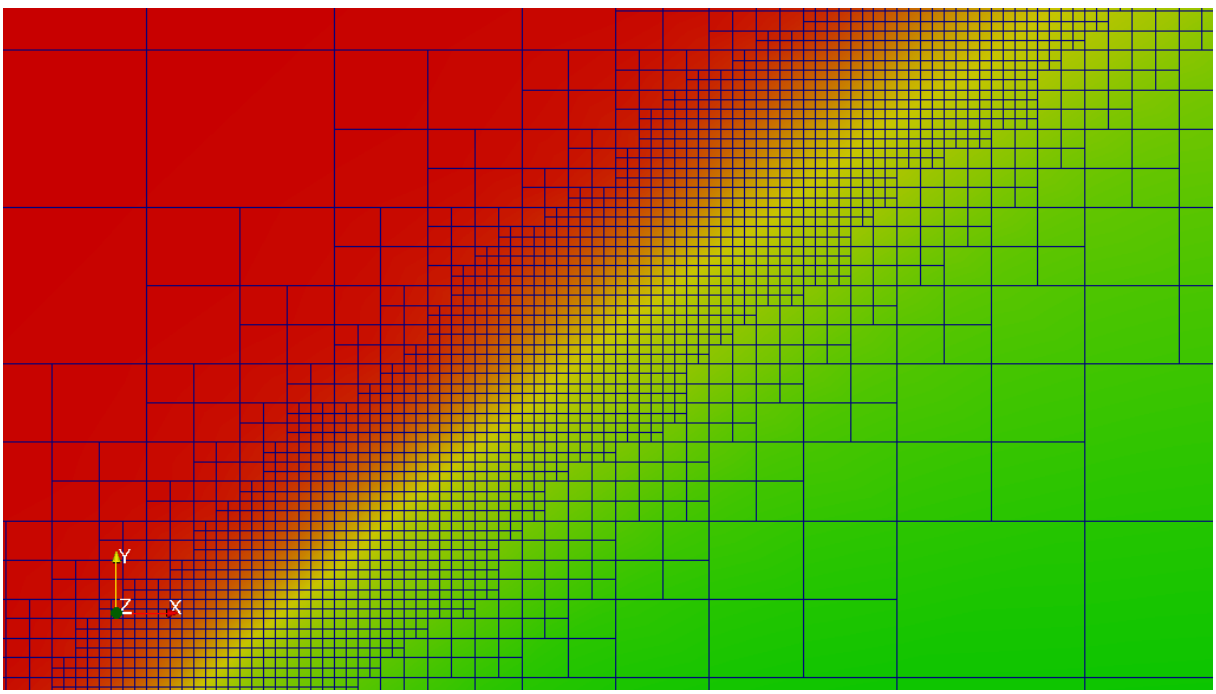

Figure 3: shock wave and the refined mesh - the solution is generated with the adaptive mesh solver

The solver splits a selected cell into 2^3 subcells. A further refinement of subcells could not be done before the next refinement interval. In this way the solver keeps large cells as long as possible and refines only critical regions. The example, see figure 3, shows this behavior of the solver. At the shock wave, each cell is highly resolved with maximum 2^{12} subcells.
The last refinement option defines the absolute cell limit. The cell limit of the present cases is set to 10^6 for a 2D-simulation and $6 \cdot 10^6$ for a 3D-simulation. The limiting factor of the cell limit is the the random access memory [RAM] of the system.
Another feature of the solver is the unrefinement of subcritical subcells. In this way, the dynamics of compressible supersonic gas flows can be qualified. If the mesh refinement is coupled to the density gradient, the cell refinement will follow the compression shocks.

4 RESULTS AND DISCUSSION

The first simulations were conducted for a first estimation of the flow field. The mesh geometry is approximated to the contour of the existing experimental setup. For the first results axis-symmetric-wedge boundary conditions were used. The used boundary conditions for inlet, outlet and internal field are given below, see table 2. The boundary conditions for pressure and temperature at the inlet and outlet are quantified by the experiments.

boundary conditions of the simulation			
term	inlet	outlet	initial field
velocity	$(\nabla\vec{v})\cdot\vec{n}=\vec{0}$	$(\nabla\vec{v})\cdot\vec{n}=\vec{0}$	$\vec{0}$
pressure	4000 Pa	50 Pa	50 Pa
temperature	300 K	300 K	300 K

Table 2: boundary conditions

The correlation of the numerical and the experimental results are presented in figure 4. The upper figure a) shows the velocity of the flow field, the central b) shows the pressure and the lower c) the operating experimental setup.

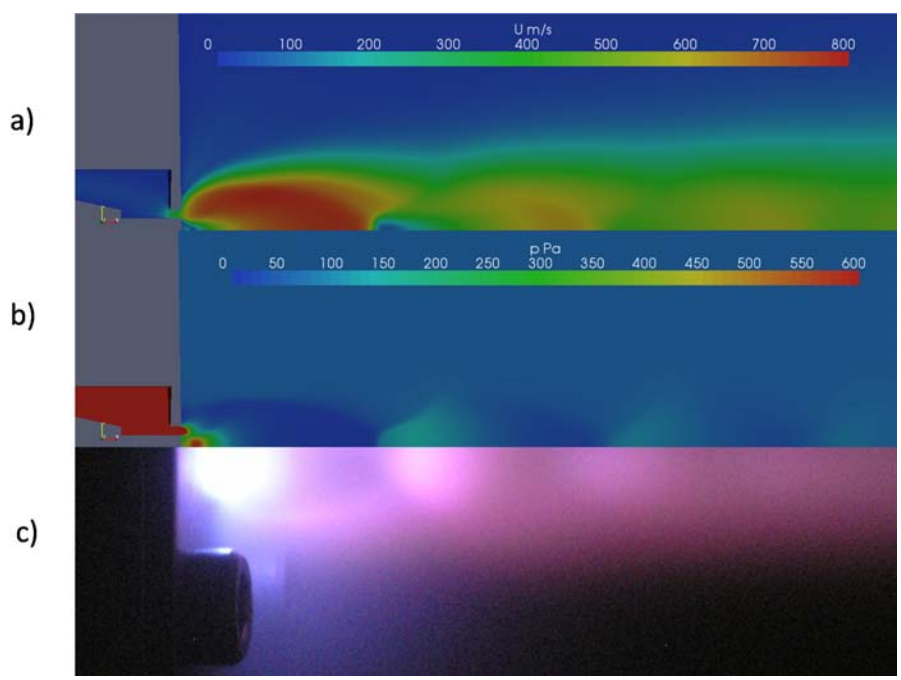

Figure 4: velocity and pressure fields in comparison with plasma illumination experimental data

In this figure, the pressure field is contrasted to illuminance of the experimental flow

field. The reason for this selection is that directly behind the ring-shape gap the illuminance of the experimental flow field is proportional to the initiated gas density.

The pictures of the experiments and the numerical results are in good agreement although the numerical solver does not consider electrical volume forces. The reason for the good agreement is that the electrical volume forces are too low for a quantifiable influence. The major advantage of the electrical current through the flow field is the visualization of the flow field.

The 3D-simulation has been conducted with the refinement solver and nearly the same boundary conditions as the 2D-simulation. Only the axis-symmetric boundary conditions are replaced as they are not necessary in a 3D-simulation. The figure of the 3D-flow field is presented below, see figure 5. The inlet with the concentric rift is on the left hand, the outlet on the right. The pressure is 4000Pa at the inlet and 50Pa at the outlet. The figure is divided into two regions. The upper half of the figure shows a section through the flow field. The velocity magnitude is ploted in this section. The shapes behind the concentric rift show the region where the refinement tool has subdevided the basic cells into subcells. The lower half of the figure shows stream tracers for the visualization of the movements inside the flow field. The stream tracers are colored due to varying pressure.

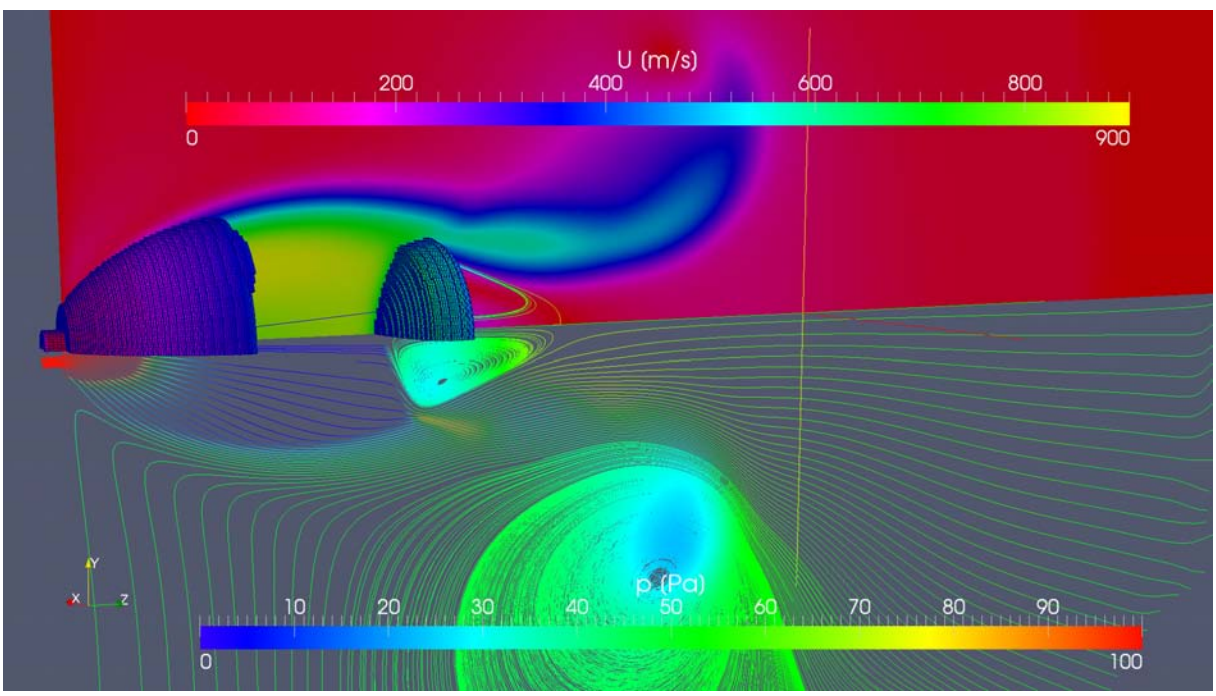

Figure 5: final 3D-simulation - including adaptive meshes - shown are velocity (top) and presure (bottom)

The flow field illustrated in figure 5 is taken after 0.2 ms. That is the reason for the unsteady solution. The steady state solution is achived after 4 ms, see figures 6-10.

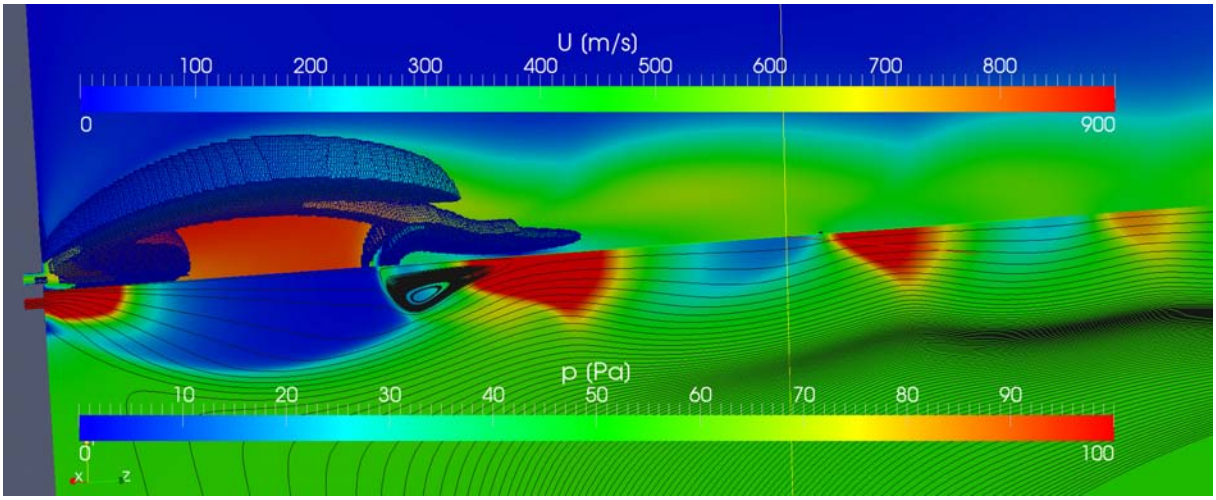

Figure 6: final 3D-simulation - steady state solution - of velocity (top) and pressure (bottom) after 0.4 ms

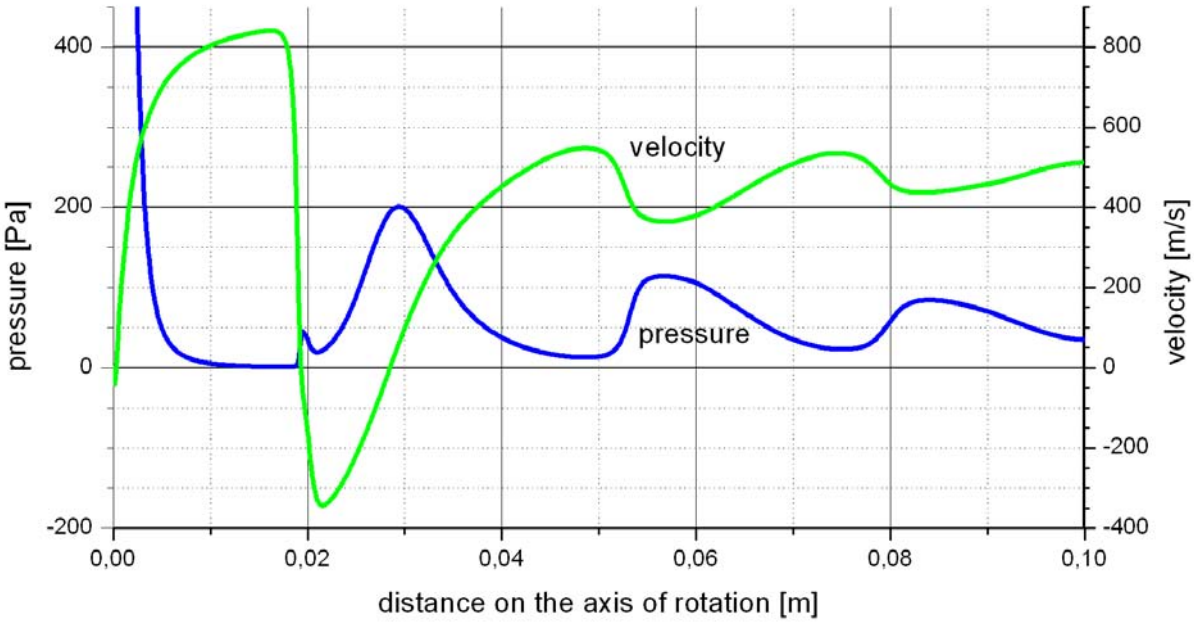

Figure 7: velocity and pressure in dependence on the virtual axis of rotation

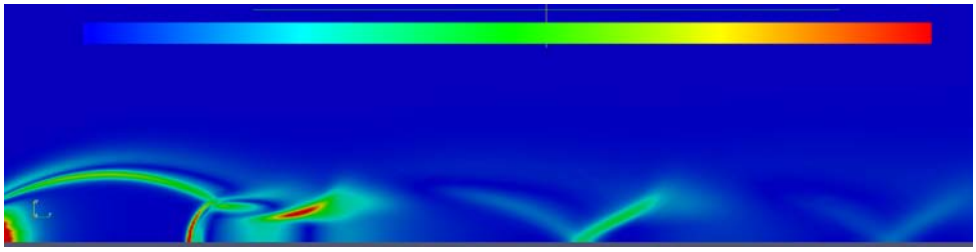

Figure 8: final 3D-simulation - steady state solution - $\nabla\rho$ is used as threshold for the refinement tool after 0.4 ms

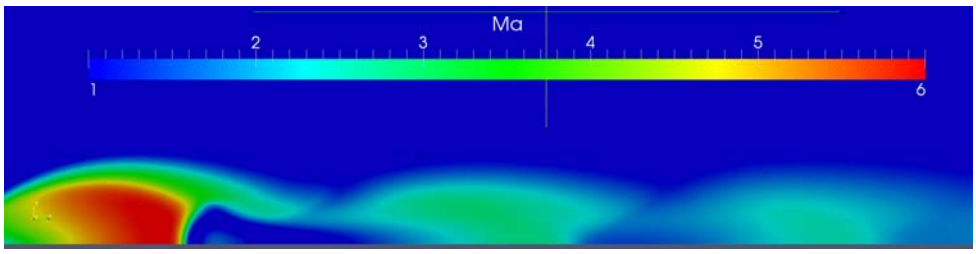

Figure 9: final 3D-simulation - steady state solution - Mach number after 0.4 ms

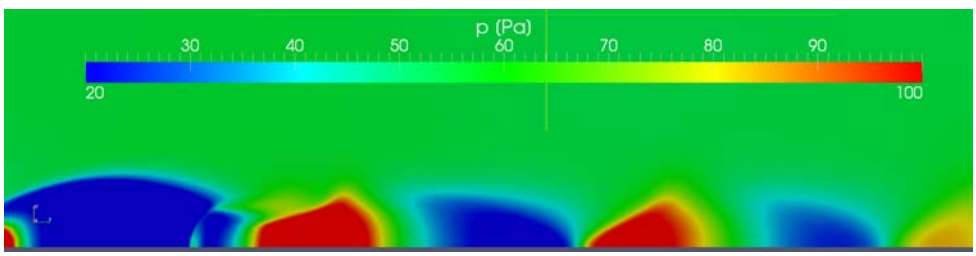

Figure 10: final 3D-simulation - steady state solution - pressure along virtual axis of rotation after 0.4 ms

As shown on the plots 4 and 6, along the virtual axis of rotation the pressure and the velocity depend on the distance to the concentric rift. To decelerate this effect a close look to the flow field is neeeded. Behind the concentric rift, the velocity increases whereas the pressure decreases, until the pressure is nearly zero. At this point, the local velocity is at its maximum. Direct, behind this point, the pressure increases and the velocity decrease and a node of high density (pressure) emerged. This behavior is presented in the plot of flow, see figure 7. This plot shows the pressure behind the concentric rift along the z-axis (virtual axis of rotation). The plot figure 8, shows the density gradient $\nabla\rho$. The density gradient is the threshold for the mesh refinement tool. The regions, which are green, yellow and red colored, are the regions where the refinement tool has subdevided the basic mesh into subcells. Operator $\nabla\rho$ is adapted for the detection of compression waves inside a flow field. In figure 9 Mach number is illustrated. The subsonic regions are blue colored, red is Mach 6. The last figure shows the pressure in correspondence to the other two plots. All three figures are taken after 4ms simulation time, where the solution is steady state.

5 CONCLUSIONS

The adaptive mesh refinement tool is able to increase the local number of cells. In this way the system sources are used very efficient. The region of interest could be refined by the definition of a suitable threshold. The basic wide-meshed mesh is sufficient for the numerical solver. The quality of the solution is depending on the suitable refinement threshold and the cell limits.
The results considered here show:

- Adaptive mesh refinement is well adequate tool for the generation of high resolved numerical solutions.
- A general advantage of the adaptive esh solver is the more efficent use of sources compared to tue common numerical solver.
- The solver works only in a 3D systems. Symmetric boundary conditions are illegal.

REFERENCES

[1] T.S.Sheshadri, Anode surface temperature profile in MPD thrusters *Vacuum, Vol. 59, 2000, Holon Academic Institute of Technology* P.O. Box 305, Holon 58102, Israel; January 2003

[2] Choueiri, On the Thrust of Self-Field MPD Thrusters *IEPC-97-121, Electric Propulsion and Plasma Dynamics Laboratory (EPPDyL)* Princeton University; 1997

[3] R. Groll Computational Modelling of molecular Gas Convection with a c2z2-Model *ASME electronic publication ASME-I793CD*, ISBN 0-7918-3826-9, 2008

[4] Roger M. Myers Scaling of 100 kW Class Applied-Field MPD Thrusters*Sverdrup Technology, Inc., Lewis Research Center Group, 2001 Aerospace Parkway, Brook Park, Ohio 44142*, July 1992

[5] A. Fruchtman Limits on the efficiency of several electric thruster configurations *PHYSICS OF PLASMAS, Vol. 10, MAY 2003; Department of Aeronautics and Astronautics* University of Southampton, Highfield, Southampton, Hampshire, SO17 1BJ, UK; August 1997

[6] W. Sutherland The viscosity of gases and molecular force*Philosophical Magazine, S. 5, 36, pp. 507-531 (1893)*

[7] H. Oertel, M. Böhle, U. Dohrmann Strmungsmechanik *Vieweg + Teubner, 5., berarbeitete und erweiterte Auflage, ISBN 978-3-8348-0483-9; GWV Fachverlage GmbH, Wiesbaden 2009*